BIOCHEMISTRY
including biophysical chemistry & molecular biology

Article

pubs.acs.org/biochemistry

Permeation of Styryl Dyes through Nanometer-Scale Pores in Membranes

Yao Wu,[†] Liang Ma,[‡] Stephen Cheley,[§] Hagan Bayley,[§] Qiang Cui,[‡] and Edwin R. Chapman*,[†]

[†]Howard Hughes Medical Institute and Department of Neuroscience and [‡]Department of Chemistry and Theoretical Chemical Institute, University of Wisconsin, Madison, Wisconsin 53706, United States

[§]Department of Chemistry, University of Oxford, Oxford OX1 3TA, England, U.K.

Supporting Information

ABSTRACT: Styryl dyes are widely used to study synaptic vesicle (SV) recycling in neurons; vesicles are loaded with dye during endocytosis, and dye is subsequently released via exocytosis. During putative kiss-and-run exocytosis, efflux of dye from individual SVs has been proposed to occur via two sequential steps: dissociation from the membrane followed by permeation through a small fusion pore. To improve our understanding of the kinetics of efflux of dye from vesicles during kiss-and-run events, we examined the rates of efflux of different dyes through nanometer-scale pores formed in membranes by the toxins melittin and α-hemolysin; these pores approximate the size of fusion pores measured in neuroendocrine cells. We found that the axial diameter of each dye was a crucial determinant for permeation. Moreover, the two dyes with the largest cross-sectional areas were completely unable to pass through pores formed by a mutant α-hemolysin that has a slightly smaller pore than the wild-type toxin. The overall time constant for efflux (seconds) of each dye was orders of magnitude slower than the time constant for dissociation from membranes (milliseconds). Thus, the permeation step is rate-limiting, and this observation was further supported by atomistic molecular dynamics simulations. Together, the data reported here help provide a framework for interpreting dye destaining rates from secretory vesicles.

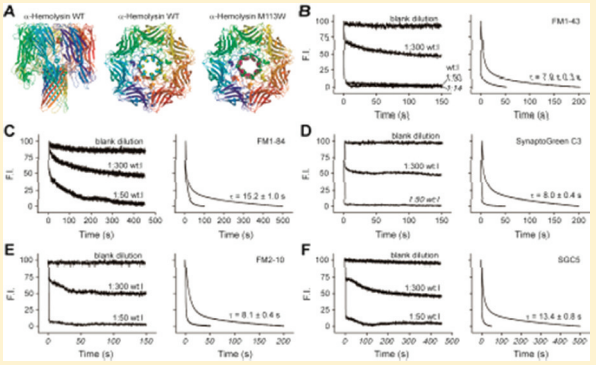

Secretion from neurons and neuroendocrine cells is a complex process that culminates in the fusion of secretory vesicles with the plasma membrane. Exocytosis proceeds through a crucial intermediate termed the fusion pore, in which a transient aqueous connection is formed between the vesicle lumen and the extracellular space. Once the fusion pore opens, it has been proposed that it has at least two fates, each of which gives rise to a distinct mode of secretion.[1−4] In one case, the pore dilates, resulting in the complete collapse of the vesicle into the plasma membrane, and this process is termed full fusion.[5] In the other case, the fusion pore is thought to undergo a reversal from the open state back to the closed state; this would occur without the complete collapse of the vesicle into the plasma membrane and is often termed "kiss-and-run" exocytosis.[6] During kiss-and-run exocytosis, the small size of the fusion pore might limit the rate of secretion. Slow transmitter efflux rates could potentially drive receptor desensitization, rather than activation,[2,7] as evidenced by a recent study focused on cultured hippocampal neurons.[8] In addition, detailed analysis of secretion from chromaffin cells revealed that kiss-and-run fusion pores act as "size exclusion" filters[9] by allowing the escape of smaller hormones but retaining larger hormones that can be released only via a subsequent full fusion event.

Kiss-and-run events are well-established for large dense-core vesicle (LDCV) exocytosis in neuroendocrine cells and cell lines and have been studied in detail via carbon fiber amperometry[4,10−12] and capacitance measurements.[2,13−15] However, whether kiss-and-run exocytosis occurs during SV exocytosis in neurons has been a subject of debate,[8,16−22] although recent experiments, using quantum dots, have provided direct and compelling evidence of kiss-and-run exocytosis in hippocampal neurons.[23] The emerging consensus is that kiss-and-run exocytosis occurs in central synapses, but whether this is a common or relatively rare mode of exocytosis remains unclear and is likely to depend upon the specific synapse under study.

The lipophilic styryl dye FM1−43, along with a number of structurally related variants that comprise the FM dye family, are widely used to study endo- and exocytosis of recycling SVs in intact neurons.[1,7,8,16,17,24] The dramatic increase in the fluorescence of these dyes that occurs when they bind to membranes can serve as an index of how much dye is incorporated into the membrane.[25] Hence, these dyes provide a quantitative tool for studying vesicle dynamics in presynaptic nerve terminals. The rate and extent of loss of dye from vesicles undergoing exocytosis can, in principle, be used to determine the mode of exocytosis.

Received: April 24, 2011
Revised: August 1, 2011
Published: August 4, 2011

A study by Richards et al.[7] suggested a simple pore permeation model for small, slow dye destaining events, interpreted to be kiss-and-run exocytosis, of FM1−43 escaping from individual SVs in hippocampal boutons. This process can be viewed as two sequential steps. (1) Membrane-bound dye molecules dissociate from the lipid membrane, and (2) free dye molecules within the vesicle lumen permeate through the open fusion pore.[7] Because our previous studies[7,25] revealed that all members of the FM dye family departition from membranes at rates (time constants in the millisecond range) that are orders of magnitude faster than their overall destaining rates from presynaptic nerve terminals (time constants in the second range),[1,7,26] we suggested that the second step, permeation, was rate-limiting. If the pore is on the order of 1−2 nm, as it is in some neuroendocrine cells,[2,4,10,13,21,27−29] the size of the dye, relative to the size of the pore, is likely to represent a crucial parameter that determines the efflux rate. Hence, under conditions of full fusion, different dyes would be expected to exhibit similar destaining rates, whereas during kiss-and-run exocytosis, smaller dyes would be expected to more readily leave vesicles (via nanometer-scale fusion pores) as compared to those with larger axial cross-sectional areas.

An earlier study employed melittin to empirically determine the kinetics of efflux of FM1−43 through small pores in membranes.[7] Even though the structures of melittin pores have not been definitively determined, a number of studies suggest that this pore is toroidal and might be lined, at least partially, with lipids.[30] There are two hypothesized models for the structure of secretory vesicle fusion pores: the lipidic pore and the protein-lined pore;[13,27] thus, melittin simulates aspects of the lipidic fusion pore. However, we note that the diameter of melittin pores is somewhat heterogeneous, this parameter varies as a function of melittin concentration,[31,32] and melittin pores are only ∼4 nm long[33] as compared to fusion pores in cells that must initially span two bilayers. So, to address these concerns and to generate pores that simulate putative protein-lined fusion pores during kiss-and-run exocytosis,[34] we also utilized α-hemolysin (αHL), which forms longer proteinaceous pores whose structure has been determined at atomic resolution.[35] By measuring the rates of efflux of different dyes through both kinds of pores in vitro, we gained a detailed understanding of how sensitive dye permeation rates are to pore diameter. Finally, our empirical findings were bolstered by complementary molecular dynamics (MD) simulations in which the free energy, and diffusion constant profiles, for permeation of FM1−43 through wild-type and mutant αHL pores were computed. These data were then used to estimate the translocation time for passage of FM1−43 through these pores, based on a mean first-passage time analysis.

MATERIALS AND METHODS

Dyes. FM1−84, FM1−43, and FM2−10 were obtained from Invitrogen (Carlsbad, CA). SynaptoGreen C3 and SGC5 were synthesized by F. Mao (Biotium, Inc.). The structure of each dye is shown in Figure S1 of the Supporting Information.

Expression and Purification of Wild-Type and Mutant αHL. Wild-type αHL was expressed, purified, and assembled into heptamers as described previously.[36] The pT7-αHL-M113W (αHL RL2) plasmid was generated by mutating the αHL RL2 gene in a pT7 vector[37] (see the Supporting Information for details).

Liposomes. 1,2-Dioleoyl-*sn*-glycero-3-phosphoethanolamine (PE) and 1,2-dioleoyl-*sn*-glycero-3-phosphocholine (PC) were from Avanti Polar Lipids (Alabaster, AL). Lipids, stored in chloroform, were dried under a stream of nitrogen and then subjected to vacuum for 1 h. Dye-containing liposomes were made by resuspending the dried lipid film (30% PE/70% PC) in HEPES buffer [50 mM HEPES and 100 mM NaCl (pH 7.4)] with dye, followed by extrusion using a 100 nm filter, resulting in dye-loaded liposomes with a mean diameter of 130 nm.

Measurement of Rates of Efflux of Dye through Pores. FM dye-containing liposomes were incubated with melittin (Sigma, St. Louis, MO) at melittin:lipid ratios of 1:10, 1:20, and 1:800 for 5 min in the presence of "external" dye, as described in a previous study,[7] to allow melittin pores to form without loss of trapped dye. The liposome·FM dye mixtures were first diluted by hand, and changes in fluorescence intensity were monitored using a PTI (South Brunswick, NJ) QM-1 spectrophotometer. After optimization of toxin:lipid ratios, dye efflux was time-resolved using an Applied Photophysics (Leatherhead, Surrey, U.K.) SX 18 MV stopped-flow spectrometer at room temperature as described previously.[25] The fluorescence changes were well fitted by single-exponential functions using GraphPad (La Jolla, CA) Prism 3. Rates are reported as time constants.

To produce pores with different structures and diameters, we also utilized the wild type and an M113W mutant form of αHL,[37] at toxin:lipid molar ratios of: 1:14, 1:50, and 1:300. To form pores, toxins and vesicles were incubated for 1 h at 37 °C; experiments were then conducted at room temperature. We examined dyes that, as shown in a previous study,[7,25] yield strong fluorescence signals; these dyes are FM1−43 (4 μM), FM1−84 (4 μM), SynaptoGreen C3 (30 μM), FM2−10 (50 μM), and SGC5 (2 μM).[25]

System Setup for MD Simulations. The crystal structure of wild-type αHL (Protein Data Bank entry 7AHL[35]) was taken as the starting structure for all simulations. Hydrogen atoms were added to the crystal structure with the HBUILD module[38] in CHARMM[39] to create an all-atom model. To generate a model for the M113W mutant, residue Met113 on each of the seven subunits of the wild-type structure was replaced with a tryptophan (Trp). Before MD simulations, the protein was first reoriented such that the longest dimension lied along the z direction and the center of mass (COM) of the transmembrane region was at $z = 0$ nm (see Figure 4A). After the reorientation, the diffusion pore ranged from approximately −2.0 to 8.0 nm in length, with a total length L of ∼10.0 nm;[35] residue M113 was at $z \sim 2.0-2.5$ nm.

The protein atoms were described with the all-atom CHARMM 27[40] force field. For FM1−43, a force field was constructed by recommended procedures for CHARMM force field development; i.e., force field parameters from chemically similar groups in CHARMM 27 were used. Specifically, parameters for amine groups were adopted from those of lipid headgroups; parameters for the six-membered ring-containing nitrogen were adopted from those of the NADP molecule, and parameters for the benzene ring and ethylene group were available in CHARMM 27. This scheme ensured compatibility between parameters for FM1−43 and those for protein and water. All bonds involving hydrogen atoms were constrained using the SHAKE algorithm[41] to allow a time step of 2 fs.

Because of the large size of αHL, only part of the system was allowed to move during the simulation, which is justified because diffusion of FM1−43 does not directly implicate a large number of protein atoms. Depending on the range of z, either

the generalized boundary solvent potential (GSBP)[42,43] or an implicit solvent method GBSW[44] was applied to treat long-range electrostatic interactions.

For the region with z values between −2.0 and 4.1 nm, the diffusion pore was relatively narrow, and a GSBP setup was applied. The system was partitioned into two regions: a rectangular inner region with x, y, and z dimensions of 3.6, 3.6, and 10.0 nm, respectively, and the remaining portion of the system as the outer region. The z of the inner region ranged from −4.0 to 6.0 nm (as shown in Figure 4A), and this region was solvated with explicit water molecules described with the modified TIP3P model.[45] All atoms in the inner region were subjected to a weak GEO type of restraining potential to keep them inside the inner rectangular box with the MMFP module of CHARMM; the effect of restraints on most inner region atoms was negligible and significant to only those within 0.2 nm of the inner−outer boundary. The outer region atoms were fixed during the simulations. The static field due to the outer region atoms and the reaction field matrix for the inner region atoms were evaluated with the linear Poisson−Boltzmann approach using a focusing scheme. In the Poisson−Boltzmann calculations, the dielectric constant of the protein and implicit membrane (treated as a dielectric slab) was set to 1, with a value of 80 for water; the salt concentration was set to 0 M. The optimized radii of Roux and Nina[46,47] were adopted to define the solvent−protein dielectric boundary. NVT simulations were conducted with the temperature controlled using the Nose-Hoover scheme.[48,49]

For the region with z values between 3.8 and 8.0 nm, the diffusion pore was relatively wide, and an implicit solvent model GBSW[44] was applied. Protein atoms more than 1.4 nm from the dye were fixed during the simulations, which were coupled via Langevin dynamics to a thermal bath at 300 K with a friction coefficient γ of 10 ps^{-1}. The dielectric map and salt concentrations in the GBSW setup were the same as those in the GSBP setup.

Estimating the Axial Diameters of FM Dyes. Geometries were first optimized in the gas phase with an approximate density functional method (SCC-DFTB[50]). The optimized structures were then simulated in the gas phase with SCC-DFTB using Nose-Hoover molecular dynamics at 300 K for 100 ps. The last 80 ps trajectories were used to obtain averaged structures of the dye molecules; the axial diameter for each dye was estimated on the basis of moment of inertia calculations for the average structure, augmented by the van der Waals radii for carbon atoms. The estimated axial diameters, at the thickest point of each dye, were 1.16 nm for FM1−84, 1.10 nm for FM1−43, 1.04 nm for SynaptoGreen C3, and 1.03 nm for FM2−10; the standard deviation in each case was 0.02 nm. These structures are shown in Figure S2 of the Supporting Information.

Free Energy Simulations. Umbrella sampling was employed to compute the one-dimensional free energy profiles $W(z)$ for the translocation of FM1−43 through the diffusion pore along the z direction. The umbrella potential was applied to the z coordinate of the COM of FM1−43, and the force constant was 200 kcal mol^{-1} nm^{-2}. In total, more than 100 windows were used to cover the range of z between −2.0 and ∼8.0 nm. The weighted histogram analysis method (WHAM)[51,52] was used to obtain $W(z)$.

For the region with z values between −2.0 and 4.1 nm (with the GSBP setup), long simulations were performed to ensure sufficient convergence of $W(z)$ because the limiting barrier of $W(z)$ fell in this region. For each window, a 1 ns equilibration simulation was conducted before 1.3 ns of production run. To monitor the convergence of $W(z)$, results using the entire 1.3 ns data were compared with those using only the first 500 ps of the production run (see Results).

For the region with z values between 3.8 and 8.0 nm (with the GBSW setup), shorter simulations were conducted because as shown below, the fine details of $W(z)$ in this region did not affect the overall translocation time. For each window, a 300 ps equilibration simulation was conducted as follows by a 500 ps production run. To monitor convergence of $W(z)$, results using the entire 500 ps data were compared with those using only the first 300 ps of the production run (see Results).

Calculation of Translocation Time. The translocation time of FM1−43 was estimated on the basis of the mean first passage time, which was calculated on the basis of $W(z)$:[53,54]

$$t = \int_0^L dz\, e^{W(z)/k_BT} D(z)^{-1} \int_0^z dz'\, e^{-W(z')/k_BT} \quad (1)$$

where L (∼10.0 nm) is the length of the pore, k_B the Boltzmann constant, and T the absolute temperature. $D(z)$ was the z-dependent diffusion constant, which could be extracted from the umbrella sampling simulations on the basis of an analysis of the velocity autocorrelation function in the framework of the generalized Langevin equation (GLE).[55] In these simulations, $D(z)$ was found to be largely z-independent, and a uniform value of 7.0 nm^2/ps was used.

RESULTS

Efflux of Styryl Dye from Vesicles through Nanometer-Scale Pores. In this study, we have focused on FM1−84, FM1−43, SynaptoGreen C3, and FM2−10, which share an identical fluorophore core; their only structural differences lie in the length of their lipophilic tails. Because the tails are branched, longer tails give rise to larger axial diameters; these values were estimated as described in Materials and Methods (see also Figures S1 and S2 of the Supporting Information for dye structures). In addition, we characterized another, new, lipophilic fluorescent dye, SGC5, which has a structure that is distinct from that of styryl dyes. SGC5 gives rise to good Signal-to-Noise ratio and might prove useful for single-vesicle destaining experiments.[25]

To begin to understand the factors that influence the kinetics of efflux of dye through fusion pores, we made use of pores formed in artificial liposomes (30% PE/70% PC) by first using melittin.[7] Melittin is a toxin peptide, produced by honeybees, that forms pores with average diameters of ∼1.3−2.4 nm in membranes; these pores are likely to be partially or completely lipidic.[30,31] Artificial liposomes were formed in the presence of dye molecules such that dye was bound to both the internal and external leaflets of the bilayer. To allow pores to become fully formed, the liposomes were incubated with melittin for 5 min at room temperature. Dye-containing liposomes were then rapidly diluted in buffer, and the loss of fluorescence was monitored using a spectrofluorometer (Figure 1A). One component of the decrease in the magnitude of the fluorescence signal was due to the dissociation of dye molecules from the external leaflet of the liposomes. This occurred rapidly, on the millisecond time scale,[7,25] which made it too fast to be detected in these hand mixing experiments. The second, slower, component was due to loss of dye molecules from the

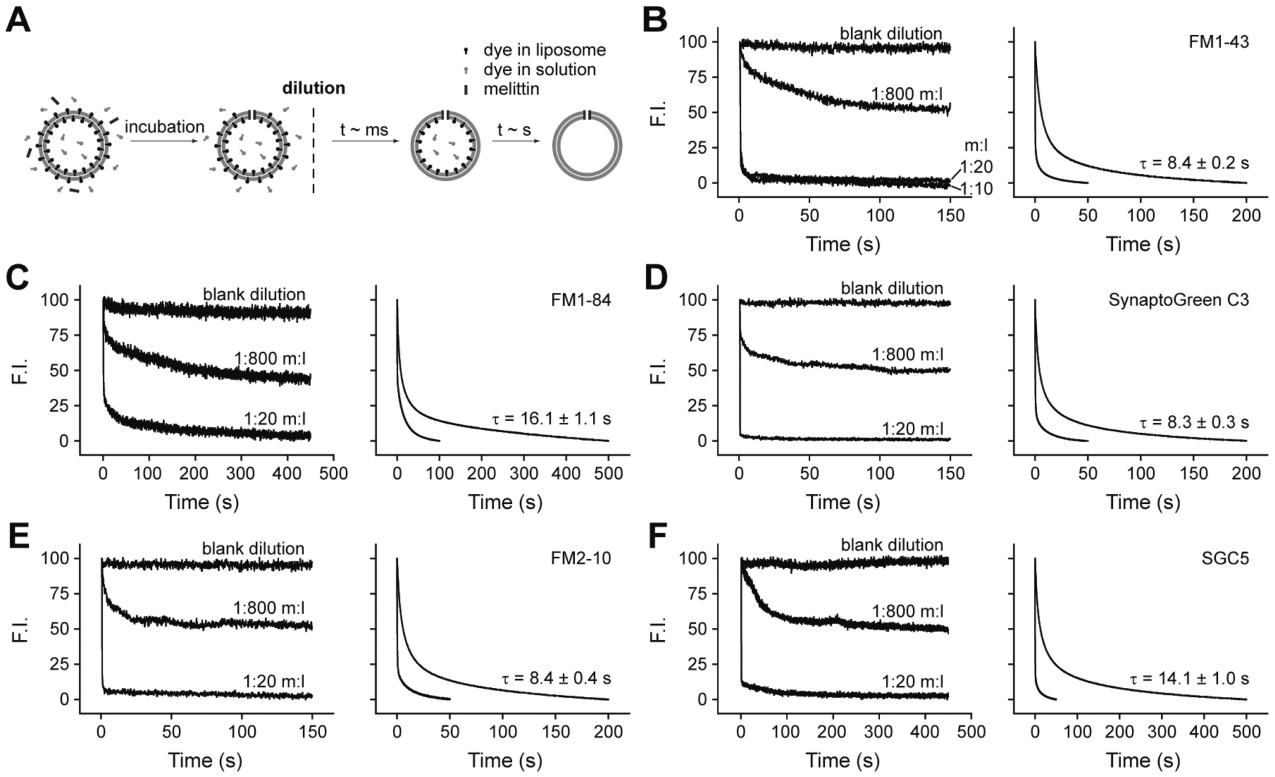

Figure 1. Efflux of dyes through melittin pores. (A) Outline of the experimental procedure used to monitor efflux of dye from liposomes. (B–F) Left panels show sample traces from hand mixing experiments showing efflux of FM1–43, FM1–84, SynaptoGreen C3, FM2–10, and SGC5 through fully assembled melittin pores. The blank dilution trace indicates samples that were diluted in the absence of pore-forming toxin. The molar ratios of melittin to lipid (m:l) were 1:800, 1:20, and 1:10. F.I. denotes fluorescence intensity in arbitrary units. (B–F) Right panels show dye efflux was time-resolved using a rapid mixing stopped-flow spectrometer. The top traces and bottom traces are from samples with 1:800 and 1:20 m:l ratios, respectively. τ values are the means ± the standard error from three separate experiments. All kinetic traces were normalized.

Table 1. Efflux Time Constants (in seconds) for Nanometer Pores

	FM1–84	FM1–43	SGC3[a]	FM2–10	SGC5
melittin	16.1 ± 1.1	8.4 ± 0.2	8.3 ± 0.3	8.4 ± 0.4	14.1 ± 1.0
αHL-wt	15.2 ± 1.0	7.9 ± 0.3	8.0 ± 0.4	8.1 ± 0.4	13.4 ± 0.8
αHL-M113W	–	34.7 ± 3.6	29.3 ± 3.1	20.5 ± 2.8	–

[a]SynaptoGreen C3.

inside of the liposome; these dye molecules are likely to first departition from the interior membrane followed by permeation through the nanometer-scale pores formed by melittin, which occurred on the seconds time scale (Figure 1A). However, we note that some degree of lateral diffusion of the dyes, through the potentially lipidic melittin pores, cannot be ruled out.

The first goal was to find conditions in which liposomes harbor, on average, a single pore, so that the rates of efflux though individual pores could be determined. To this end, we titrated melittin onto dye-loaded vesicles. When the melittin:lipid ratio was increased from 1:800 to 1:20, there was a greater loss of fluorescence, presumably because the formation of pores in all liposomes when more melittin was used (Figure 1B). This conclusion was supported by the finding that the loss of fluorescence reached a limit, and no further drop was observed at a ratio of 1:10 (Figure 1B); hence, a melittin:lipid ratio of 1:20 should be sufficient to induce pore formation in virtually every liposome. At a melittin:lipid ratio of 1:800, one-half of the total fluorescence signal was lost (Figure 1B), indicating that roughly 50% of the liposomes harbored one pore with the other 50% of the vesicles devoid of pores (assuming efficient mixing of melittin and liposomes and assuming that the pores do not associate with one another). We then examined the kinetics of dye efflux under these conditions (melittin:lipid ratio of 1:800) in a stopped-flow spectrometer, using each of the five dyes. With melittin, the efflux rates of FM1–84 and SGC5, which possess relatively long five-carbon tails, were significantly slower than those of the other three smaller dyes. Interestingly, the three smaller dyes, FM1–43, SynaptoGreen C3, and FM2–10, all exhibited similar efflux kinetics (Figure 1 and Table 1). These data confirm an earlier study focused on FM1–43[7] and also indicate the existence of a critical threshold regarding the relative diameters of the dyes relative to the pore during permeation, as detailed further below and in Discussion.

While these results are consistent with an earlier study of FM1–43, it is important to note that the stoichiometry of melittin pores remains unclear and is thought to be variable; indeed, pore size depends on the concentration of melittin used.[30−32] To address these concerns, we turned to αHL, as a proteinaceous pore. αHL is a 33.2 kDa water-soluble monomer that forms reproducible and fixed-stoichiometry heptameric

dx.doi.org/10.1021/bi2006288 | Biochemistry 2011, 50, 7493–7502

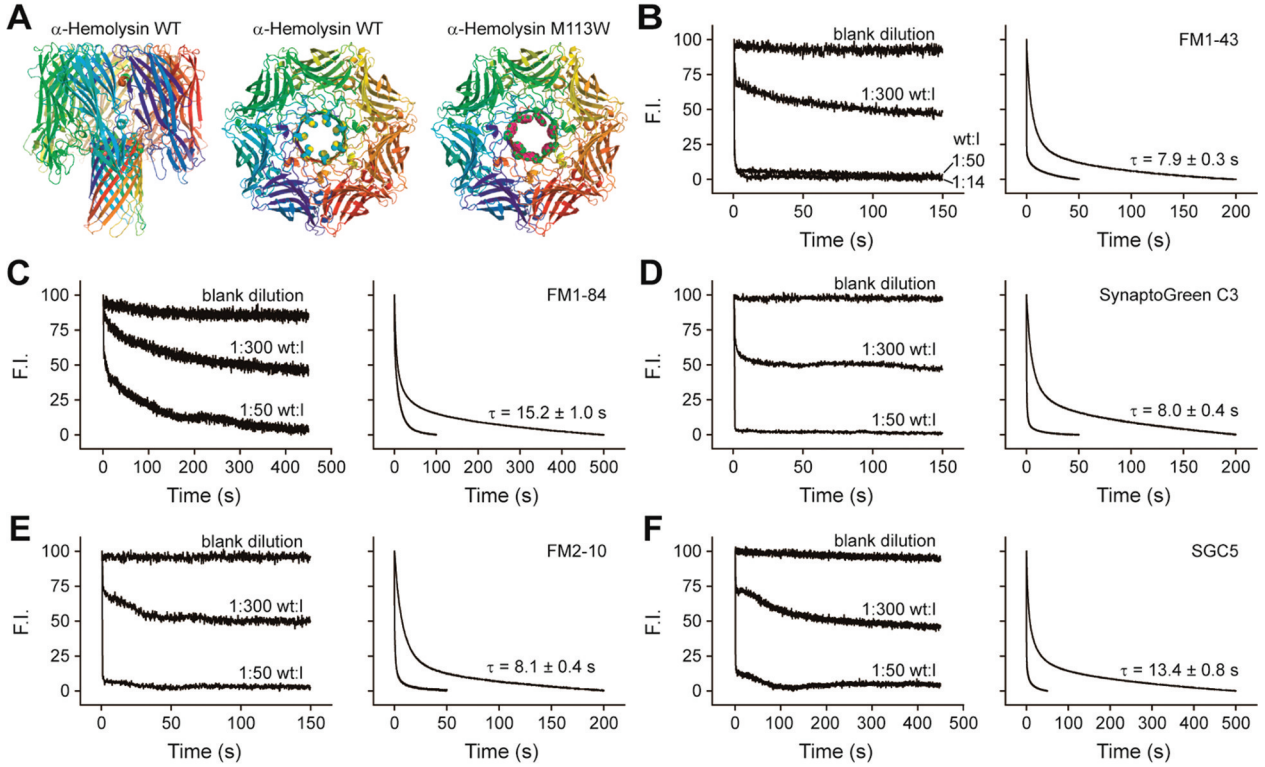

Figure 2. Efflux of dyes through αHL-wt pores. (A) Structures of wild-type and M113W mutant αHL. From left to right are shown a side view of αHL-wt, a top view of αHL-wt with a methionine at position 113 (space fill), and a top view of αHL-M113W in which tryptophan residues at position 113 are shown in space fill, respectively. Images for these structures were generated using PyMOL. (B–F) Efflux of dyes from fully assembled αHL-wt pores from hand mixing (left) and rapid mixing stopped-flow experiments (right) as described in the legend for Figure 1. In the rapid mixing experiments, the top and bottom traces harbor wild-type toxin:lipid (wt:l) ratios of 1:300 and 1:50, respectively. τ values are means ± the standard error from three separate experiments.

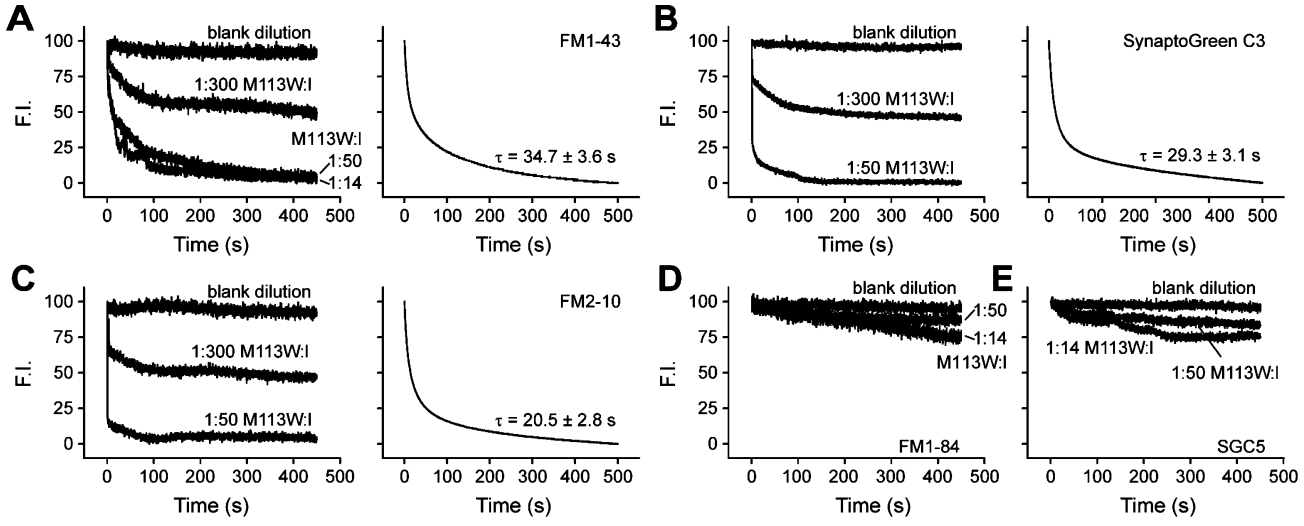

Figure 3. Efflux of dyes through αHL-M113W pores. (A–C) Efflux of FM1–43, SynaptoGreen C3, and FM2–10 from fully assembled αHL-M113W pores measured via hand mixing experiments (left) and rapid mixing stopped-flow experiments (right) as described in the legend for Figure 1. In the rapid mixing experiments, the molar ratios of mutant toxin to lipid (M113W:l) were 1:300 (top traces) and 1:50 (bottom traces). τ values are means ± the standard error from three separate determinations. (D and E) Hand mixing experiments revealed that FM1–84 and SGC5 cannot pass through fully assembled αHL-M113W pores at M113W:l ratios of 1:50 and 1:14.

pores. The crystal structure of the αHL pore has been determined, and the most narrow segment of the pore lumen has a diameter of 1.4 nm (Figure 2A).[35] To retard the efflux of dyes, Trp residues were introduced into the neck of the pore lumen, at residue M113, where the narrow segment is located (Figure 2A). It has been confirmed that the conductance of this M113W mutant form of the αHL (αHL-M113W) pore is ~20% lower than that of wild-type αHL (αHL-wt).[37]

We conducted the same experiments as described for each dye and melittin, but using αHL-wt and αHL-M113W. As

dx.doi.org/10.1021/bi2006288 | Biochemistry 2011, 50, 7493–7502

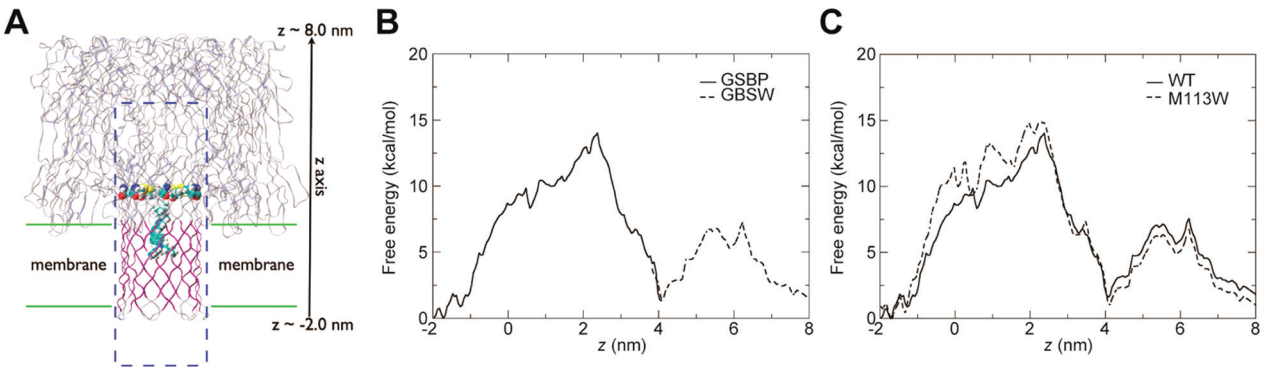

Figure 4. Simulation setup and free energy profiles. (A) Snapshot of wild-type αHL. The protein is shown in ribbon form, and the transmembrane region is colored purple. M113 and an FM1−43 molecule are shown in the van der Waals scheme. The water solvation box for the GSBP setup is shown in the box bounded by the blue dashed lines, with water molecules omitted for the sake of clarity. The figure was created using VMD.[60] (B) Comparison of free energy profiles $W(z)$ for FM1−43 diffusing through αHL-wt using two methods, GSBP and GBSW, which generate consistent $W(z)$ values in the overlapping z region between 3.8 and 4.1 nm. (C) Computed free energy profiles $W(z)$ of FM1−43 for the translocation of FM1−43 in both αHL-wt (—) and αHL-M113W (---) based on umbrella sampling simulations.

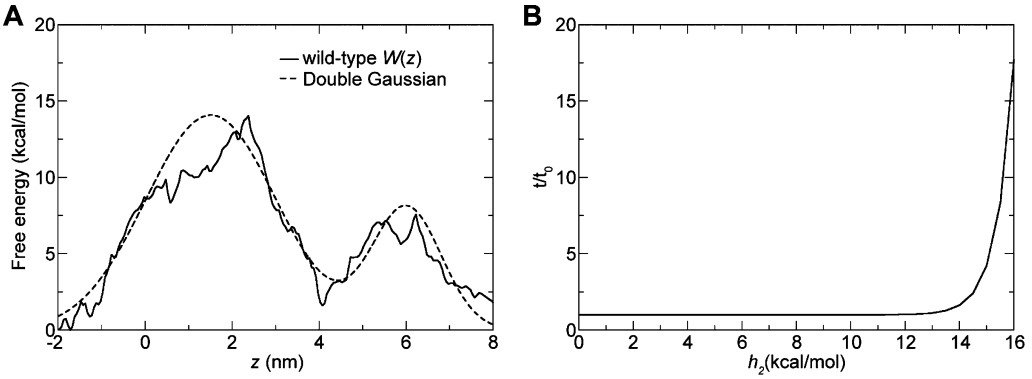

Figure 5. Insensitivity of t to the second lower barrier. (A) Fitting $W(z)$ for αHL-wt with a double-Gaussian function as given in eq 2. The double-Gaussian function gives the same translocation time as the wild-type $W(z)$. (B) t/t_0 ratio for the double-Gaussian function as a function of h_2 with fixed a h_1 of 14.08 kcal/mol.

detailed in Materials and Methods, the incubation time for wild-type and mutant αHL was 1 h at 37 °C to ensure complete pore formation. The αHL:lipid ratio for a 50% loss of fluorescence was 1:300, so this condition, in which half the vesicles have a single pore, was used in all time-resolved stopped-flow experiments (Figures 2 and 3). As with melittin pores, the efflux of FM1−84 and SGC5 through αHL-wt was significantly slower than that of the other three dyes, whereas FM1−43, SynaptoGreen C3, and FM2−10 exhibited similar efflux rates (Figure 2 and Table 1). The time constant for efflux of FM1−43 was 7.9 s, which was in line with the time constant for destaining of FM1−43 from single SVs (τ = 7.2 s) during putative kiss-and-run events in cultured hippocampal neurons.[7] Efflux of FM1−43, SynaptoGreen C3, and FM2−10 through αHL-M113W pores was much slower than through αHL-wt pores, and the efflux rates of these three dyes now differed from one another (Figure 3 and Table 1). These data again indicate that the size of the dye, relative to the size of the pore, plays a crucial role in determining the rate of efflux. This point is further underscored by the finding that FM1−84 and SGC5 failed to permeate though the smaller pores composed of αHL-M113W (Figure 3D,E).

Pores formed by αHL are similar in size to fusion pores in neuroendocrine cells,[2,4,10,13,21,27−29] and both kinds of pores are similar to the axial cross-sectional area of the styryl dyes. This coincidence, coupled to the empirical efflux rates measured above, demonstrates that flux of styryl dye from secretory vesicles will be sensitive to the dimensions of cellular fusion pores.

Free Energy Profiles and Translocation Times of FM1−43 through Wild-Type and M113W Mutant αHL As Determined from Simulations. To further analyze the influence of dye size on rates of flux through nanometer-scale pores, we conducted MD computer simulations for the free energy profiles for FM1−43 in αHL pores to estimate the translocation time. First, we checked the consistency of free energy profiles $W(z)$ calculated using GSBP[42,43] and GBSW[44] setups by comparing $W(z)$ values in the overlapping region, i.e., z between 3.8 and 4.1 nm. As shown in Figure 4B, wild-type $W(z)$ values in the overlapping region using the two methods were consistent with each other. This justified connecting $W(z)$ from the two sets of simulations to generate the complete $W(z)$ profile across the entire range of interest. $W(z)$ for αHL-M113W showed similar behavior (data not shown).

The computed $W(z)$ values for αHL-wt and αHL-M113W are shown in Figure 4C. For both systems, there were two barriers in $W(z)$, and the limiting barrier was observed around the narrowest segment of the pore (z ~ 2.0−2.5 nm), where the M113 residues (or W113 in the M113W mutant) were located. The limiting barrier was ~14 kcal/mol for αHL-wt, and it increased to ~15 kcal/mol for αHL-M113W. Because both

dx.doi.org/10.1021/bi2006288 | Biochemistry 2011, 50, 7493−7502

Met and Trp are charge neutral residues, the change in $W(z)$ is due mainly to the larger size of the Trp residues.

Next, the convergence of $W(z)$ with respect to sampling was evaluated by comparing $W(z)$ using different lengths of production runs. As shown in Figure S3 of the Supporting Information, $W(z)$ in the GSBP region had largely converged whereas $W(z)$ in the GBSW region still showed variation on the order of 2−3 kcal/mol as the simulation time was extended. However, as discussed below, the fine details of $W(z)$ in the GBSW region were not essential to the overall translocation time. In other words, the calculated $W(z)$ profiles have converged to a satisfactory degree for this purpose.

The calculated dye translocation times according to eq 1 were ∼1.3 and ∼12.7 s for αHL-wt and αHL-M113W, respectively. Encouragingly, these values agreed with experimental values of ∼8 and ∼35 s, respectively, within the same order of magnitude.

To investigate the sensitivity of the calculated translocation time to the height of the second barrier in the GBSW region, we first fitted the wild-type $W(z)$ with two Gaussian functions (see Figure 5A for the fit):

$$W_{\text{fit}}(z) = h_1 e^{(z-z_1)^2/2\sigma_1^2} + h_2 e^{(z-z_2)^2/2\sigma_2^2} \quad (2)$$

where h_1 = 14.08 kcal/mol, z_1 = 1.5 nm, σ_1 = 1.5 nm, h_2 = 8.0 kcal/mol, z_2 = 6.0 nm, and σ_2 = 0.8 nm for the best fit of the computed translocation time. We then fixed h_1 to 14.08 kcal/mol and calculated the t/t_0 ratio for different h_2 values, where t_0 was the calculated translocation time and h_2 equaled 8.0 kcal/mol. As shown in Figure 5B, t/t_0 was nearly 1 for h_2 values of ≤14 kcal/mol. This confirms the expectation that the translocation kinetics are not sensitive to the height of the second (lower) barrier. Consistent with this simple test using Gaussian functions, t values were calculated for the $W(z)$ profiles in Figure S3 of the Supporting Information on the basis of different lengths of production runs. The values were 1.7 and 1.3 s for αHL-wt and 10.7 and 12.7 s for αHL-M113W, once again confirming that the calculated translocation time was insensitive to the lower barrier and the $W(z)$ had sufficiently converged for this purpose.

DISCUSSION

To improve our understanding of how FM dyes, and SGC5, are released from presynaptic nerve terminals, we simulated putative kiss-and-run fusion pores using toxins in artificial liposomes and directly measured dye efflux rates. The structure of melittin pores remains somewhat unclear but is generally thought to be toroidal with an at least partial lipidic nature with a pore diameter that ranges from 1.3 to 2.4 nm[30,31] and was thus used to simulate lipidic fusion pores. αHL, which assembles into heptamers that form protein-lined pores in membranes [with a uniform and well-defined structure (Figure 2A)],[35] was used to simulate proteinaceous fusion pores. The length of the αHL pore is 10 nm, and the diameter ranges from 1.4 nm at the narrowest point to 4.6 nm at the widest point. The effective diameter is 1.14 nm, as estimated from conductance measurements of single heptamers.[56] Moreover, to probe the relationship between pore diameter and dye flux rates more deeply, we also examined a mutant form of αHL in which a ring of seven pore-lining residues (M113) at the neck of the pore lumen was replaced with Trp residues (Figure 2A). The conductance of the αHL-M113W pore was ∼20% lower than that of αHL-wt,[37] indicating that the effective diameter of the αHL-M113W pore is ∼1 nm.

The time constants for efflux of FM1−43 through melittin and αHL-wt pores were 8.4 and 7.9 s, which were comparable to the time constant for FM1−43 destaining from single SVs (τ = 7.2 s) during putative kiss-and-run events in cultured hippocampal neurons (ref 7, but see also ref 16). For both melittin and αHL-wt pores, the two largest dyes (FM1−84 and SGC5) exhibited the slowest efflux rates as compared to the other three smaller dyes. Interestingly, FM1−43, SynaptoGreen C3, and FM2−10 exhibited similar rates of efflux through αHL-wt pores (Table 1). It is possible that the five-carbon tails of FM1−84 and SGC5 have reached a critical cross-sectional area, resulting in a significantly larger energy barrier that must be overcome for passage through the αHL-wt pore. Indeed, the small reduction in pore diameter in αHL-M113W pores was sufficient to prevent passage of FM1−84 and SGC5 (Figure 3D,E). Moreover, the efflux rates of the three smaller dyes not only were markedly slower through the mutant pore than through wild-type pores but also now differed from one another (Table 1). These results indicate that biological fusion pores with diameters of 1−2 nm[2,4,10,13,21,27−29] have, by chance, dimensions similar to the axial cross-sectional area of the FM dyes (which we estimate to be 1.16 nm for FM1−84, 1.10 nm for FM1−43, 1.04 nm for SynaptoGreen C3, and 1.03 nm for FM2−10; see Materials and Methods for details). Hence, small changes in the diameter of the dyes, or in the diameter of the fusion pore, result in large changes in dye efflux rates.

It should be noted that lipophilic components in the synaptic cleft might also influence the destaining kinetics of these dyes from neurons. Furthermore, there is a possibility that the dyes may leave secretory vesicles in cells via lateral diffusion along lipidic pores, which might influence the kinetics of permeation. However, the data reported here demonstrate that the kinetics of efflux through melittin or αHL pores are similar, so this latter possibility does not appear to strongly affect our conclusions.

To improve our understanding of efflux, we also studied the translocation of FM1−43 in αHL-wt and αHL-M113W pores using MD computer simulations. We computed the free energy profiles of FM1−43 translocation in the pore, from which the translocation times were calculated on the basis of mean first-passage time. The calculated results were in agreement (within 1 order of magnitude) with the empirical efflux rates. Comparing the free energy profiles for αHL-wt and αHL-M113W, we confirmed that the bulky side chain of the Trp mutation increased the energetic barrier for FM1−43 diffusion, which led to the observed change in translocation time and efflux rate, again highlighting the importance of pore size when it approaches the diameter of the dye used to study flux.

Taken together, these findings indicate that the size of the dye, relative to the size of the pore, is a crucial determinant for rates of efflux through kiss-and-run fusion pores; our data strongly suggest that permeation (the second step) is the rate-limiting step, in agreement with an earlier study.[7] In contrast, the destaining rates of different dyes would be expected to be similar during full fusion. In previous studies, the destaining rates of different FM dyes (e.g., FM1−84, FM1−43, and FM2−10) from presynaptic boutons were reported to differ[1] or to be the same.[26] The reasons for these apparent discrepancies remain to be resolved. A recent study, using quantum dots, provides strong support for the notion that kiss-and-run exocytosis is a common mode of transmitter release in

hippocampal neurons.[23] According to this new study, the fraction of kiss-and-run versus full fusion events is subject to regulation; under specific conditions, one mode of exocytosis is predominant over the other, but whether the kiss-and-run mode predominates at high or low stimulation frequencies is still an open question.[18,57]

There are indications that the diameter of SV fusion pores in the calyx of Held synapse is >2.3 nm, and a small fraction have a diameter of ~1.1 nm.[19] However, fusion pores that mediate exocytosis from microvesicles in posterior pituitary nerve terminals have been reported to have a diameter of only 0.6 nm,[2] which is too small to take up or release dyes during kiss-and-run exocytosis and thus would elude detection in FM dye experiments. The diameters cited above were derived from conductance measurements obtained by capacitance experiments. This approach is not amenable to studying modes of exocytosis in central neurons with tiny boutons. Therefore, in most cases, the frequency of kiss-and-run exocytosis and the diameter of fusion pores remain unknown. Hence, it is difficult to estimate the rate of neurotransmitter flux during kiss-and-run exocytosis. This is a crucial question because, again, small pores might retard efflux of glutamate, for example, resulting in receptor desensitization rather than activation.[8] To gain insight into the structure and properties of fusion pores in central neurons, a detailed understanding of the loss of dye from SVs and from model systems is needed. The data reported here help to provide an empirical basis for interpreting dye destaining data from single SVs.

Two general hypothetical models of fusion pore structure, the lipidic pore and the protein-lined pore, have been proposed.[13,27] Han et al., using amperometry and capacitance measurements to study large dense core vesicle secretion in PC12 cells, suggest that the fusion pore is transiently lined by the transmembrane domains of multiple syntaxin molecules,[34] which is a soluble *N*-ethylmaleimide-sensitive factor attachment protein receptor (SNARE) that, together with SNAP-25 and synaptobrevin, forms the core of the fusion machinery.[58,59] Trp mutations at three sites of the transmembrane domain of syntaxin decreased the flux of transmitter and the conductance of fusion pores and would thus be predicted to retard the rate of loss of FM dye from vesicles or even prevent dye permeation during kiss-and-run events. It will therefore be of interest to analyze the rate of release of dye from vesicles undergoing exocytosis in PC12 cells to gain further insight into the structure of biological fusion pores; indeed, approximately one-quarter of release events in PC12 cells occur via a kiss-and-run mechanism.[12] It will also be interest to determine whether Trp mutations in the cognate v-SNARE protein, synaptobrevin, which is anchored in the vesicle membrane, retard dye efflux; if so, it would strongly suggest that synaptobrevin forms the other half of the fusion pore. A long-term goal will be to use the same approach to test the "SNARE-lined pore model" during kiss-and-run SV exocytosis in neurons.

■ ASSOCIATED CONTENT

Supporting Information

A detailed method of expression and purification of mutant αHL and additional figures. This material is available free of charge via the Internet at http://pubs.acs.org.

■ AUTHOR INFORMATION

Corresponding Author

*Howard Hughes Medical Institute and Department of Neuroscience, University of Wisconsin, 1300 University Ave., SMI 129, Madison, WI 53706. E-mail: chapman@wisc.edu. Telephone: (608) 263-1762. Fax: (608) 265-5512.

Funding

This work was supported by National Institutes of Health Grants MH 61876 to E.R.C. and GM071428 and GM084028 to Q.C. E.R.C. is an Investigator of the Howard Hughes Medical Institute. Computational resources were provided by the National Center for Supercomputing Applications (NCSA) Alliance Center at the University of Illinois. H.B. acknowledges support through the Royal Society-Wolfson Research Merit Award and the Medical Research Council.

■ ACKNOWLEDGMENTS

We thank F. Mao for providing SynaptoGreen C3 and SGC5 and M. Jackson and the Chapman lab for helpful discussions. We also thank Guanhua Hou for conducting the estimations of dye diameters.

■ ABBREVIATIONS

PC, 1,2-dioleoyl-*sn*-glycero-3-phosphocholine; PE, 1,2-dioleoyl-*sn*-glycero-3-phosphoethanolamine; αHL, α-hemolysin; αHL-M113W, M113W mutant form of αHL; αHL-wt, wild-type αHL; COM, center of mass; GLE, generalized Langevin equation; LDCV, large dense-core vesicle; MD, molecular dynamics; SNARE, soluble *N*-ethylmaleimide-sensitive factor attachment protein receptor; SV, synaptic vesicle; WHAM, weighted histogram analysis method.

■ REFERENCES

(1) Klingauf, J., Kavalali, E. T., and Tsien, R. W. (1998) Kinetics and regulation of fast endocytosis at hippocampal synapses. *Nature 394*, 581−585.

(2) Klyachko, V. A., and Jackson, M. B. (2002) Capacitance steps and fusion pores of small and large-dense-core vesicles in nerve terminals. *Nature 418*, 89−92.

(3) Neher, E., and Marty, A. (1982) Discrete changes of cell membrane capacitance observed under conditions of enhanced secretion in bovine adrenal chromaffin cells. *Proc. Natl. Acad. Sci. U.S.A. 79*, 6712−6716.

(4) Wang, C. T., Lu, J. C., Bai, J., Chang, P. Y., Martin, T. F., Chapman, E. R., and Jackson, M. B. (2003) Different domains of synaptotagmin control the choice between kiss-and-run and full fusion. *Nature 424*, 943−947.

(5) Heuser, J. E., and Reese, T. S. (1973) Evidence for recycling of synaptic vesicle membrane during transmitter release at the frog neuromuscular junction. *J. Cell Biol. 57*, 315−344.

(6) Fesce, R., Grohovaz, F., Valtorta, F., and Meldolesi, J. (1994) Neurotransmitter release: Fusion or 'kiss-and-run'? *Trends Cell Biol. 4*, 1−4.

(7) Richards, D. A., Bai, J., and Chapman, E. R. (2005) Two modes of exocytosis at hippocampal synapses revealed by rate of FM1−43 efflux from individual vesicles. *J. Cell Biol. 168*, 929−939.

(8) Richards, D. A. (2009) Vesicular release mode shapes the postsynaptic response at hippocampal synapses. *J. Physiol. 587*, 5073−5080.

(9) Fulop, T., Radabaugh, S., and Smith, C. (2005) Activity-dependent differential transmitter release in mouse adrenal chromaffin cells. *J. Neurosci. 25*, 7324−7332.

(10) Albillos, A., Dernick, G., Horstmann, H., Almers, W., Alvarez de Toledo, G., and Lindau, M. (1997) The exocytotic event in chromaffin cells revealed by patch amperometry. *Nature 389*, 509−512.

(11) Alvarez de Toledo, G., Fernandez-Chacon, R., and Fernandez, J. M. (1993) Release of secretory products during transient vesicle fusion. *Nature 363*, 554−558.

(12) Wang, C. T., Bai, J., Chang, P. Y., Chapman, E. R., and Jackson, M. B. (2006) Synaptotagmin-Ca^{2+} triggers two sequential steps in regulated exocytosis in rat PC12 cells: Fusion pore opening and fusion pore dilation. *J. Physiol. 570*, 295−307.

(13) Lindau, M., and Almers, W. (1995) Structure and function of fusion pores in exocytosis and ectoplasmic membrane fusion. *Curr. Opin. Cell Biol. 7*, 509−517.

(14) Lollike, K., Borregaard, N., and Lindau, M. (1995) The exocytotic fusion pore of small granules has a conductance similar to an ion channel. *J. Cell Biol. 129*, 99−104.

(15) Fernandez, J. M., Neher, E., and Gomperts, B. D. (1984) Capacitance measurements reveal stepwise fusion events in degranulating mast cells. *Nature 312*, 453−455.

(16) Chen, X., Barg, S., and Almers, W. (2008) Release of the styryl dyes from single synaptic vesicles in hippocampal neurons. *J. Neurosci. 28*, 1894−1903.

(17) Aravanis, A. M., Pyle, J. L., and Tsien, R. W. (2003) Single synaptic vesicles fusing transiently and successively without loss of identity. *Nature 423*, 643−647.

(18) Gandhi, S. P., and Stevens, C. F. (2003) Three modes of synaptic vesicular recycling revealed by single-vesicle imaging. *Nature 423*, 607−613.

(19) He, L., Wu, X. S., Mohan, R., and Wu, L. G. (2006) Two modes of fusion pore opening revealed by cell-attached recordings at a synapse. *Nature 444*, 102−105.

(20) Granseth, B., Odermatt, B., Royle, S. J., and Lagnado, L. (2006) Clathrin-mediated endocytosis is the dominant mechanism of vesicle retrieval at hippocampal synapses. *Neuron 51*, 773−786.

(21) Spruce, A. E., Breckenridge, L. J., Lee, A. K., and Almers, W. (1990) Properties of the fusion pore that forms during exocytosis of a mast cell secretory vesicle. *Neuron 4*, 643−654.

(22) Zhu, Y., Xu, J., and Heinemann, S. F. (2009) Two pathways of synaptic vesicle retrieval revealed by single-vesicle imaging. *Neuron 61*, 397−411.

(23) Zhang, Q., Li, Y., and Tsien, R. W. (2009) The dynamic control of kiss-and-run and vesicular reuse probed with single nanoparticles. *Science 323*, 1448−1453.

(24) Betz, W. J., Mao, F., and Bewick, G. S. (1992) Activity-dependent fluorescent staining and destaining of living vertebrate motor nerve terminals. *J. Neurosci. 12*, 363−375.

(25) Wu, Y., Yeh, F. L., Mao, F., and Chapman, E. R. (2009) Biophysical characterization of styryl dye-membrane interactions. *Biophys. J. 97*, 101−109.

(26) Fernandez-Alfonso, T., and Ryan, T. A. (2004) The kinetics of synaptic vesicle pool depletion at CNS synaptic terminals. *Neuron 41*, 943−953.

(27) Jackson, M. B., and Chapman, E. R. (2006) Fusion pores and fusion machines in Ca^{2+}-triggered exocytosis. *Annu. Rev. Biophys. Biomol. Struct. 35*, 135−160.

(28) Breckenridge, L. J., and Almers, W. (1987) Currents through the fusion pore that forms during exocytosis of a secretory vesicle. *Nature 328*, 814−817.

(29) Debus, K., and Lindau, M. (2000) Resolution of patch capacitance recordings and of fusion pore conductances in small vesicles. *Biophys. J. 78*, 2983−2997.

(30) Yang, L., Harroun, T. A., Weiss, T. M., Ding, L., and Huang, H. W. (2001) Barrel-stave model or toroidal model? A case study on melittin pores. *Biophys. J. 81*, 1475−1485.

(31) Matsuzaki, K., Yoneyama, S., and Miyajima, K. (1997) Pore formation and translocation of melittin. *Biophys. J. 73*, 831−838.

(32) van den Bogaart, G., Mika, J. T., Krasnikov, V., and Poolman, B. (2007) The lipid dependence of melittin action investigated by dual-color fluorescence burst analysis. *Biophys. J. 93*, 154−163.

(33) Rex, S. (1996) Pore formation induced by the peptide melittin in different lipid vesicle membranes. *Biophys. Chem. 58*, 75−85.

(34) Han, X., Wang, C. T., Bai, J., Chapman, E. R., and Jackson, M. B. (2004) Transmembrane segments of syntaxin line the fusion pore of Ca^{2+}-triggered exocytosis. *Science 304*, 289−292.

(35) Song, L., Hobaugh, M. R., Shustak, C., Cheley, S., Bayley, H., and Gouaux, J. E. (1996) Structure of staphylococcal α-hemolysin, a heptameric transmembrane pore. *Science 274*, 1859−1866.

(36) Cheley, S., Malghani, M. S., Song, L., Hobaugh, M., Gouaux, J. E., Yang, J., and Bayley, H. (1997) Spontaneous oligomerization of a staphylococcal α-hemolysin conformationally constrained by removal of residues that form the transmembrane β-barrel. *Protein Eng. 10*, 1433−1443.

(37) Gu, L. Q., Cheley, S., and Bayley, H. (2001) Prolonged residence time of a noncovalent molecular adapter, β-cyclodextrin, within the lumen of mutant α-hemolysin pores. *J. Gen. Physiol. 118*, 481−494.

(38) Brunger, A. T., and Karplus, M. (1988) Polar hydrogen positions in proteins: Empirical energy placement and neutron diffraction comparison. *Proteins 4*, 148−156.

(39) Brooks, B. R., Bruccoleri, R. E., Olafson, B. D., States, D. J., Swaminathan, S., and Karplus, M. (1983) Charmm: A program for macromolecular energy, minimization, and dynamics calculations. *J. Comput. Chem. 4*, 187−217.

(40) MacKerell, A. D., Bashford, D., Bellott, M., Dunbrack, R. L., Evanseck, J. D., Field, M. J., Fischer, S., Gao, J., Guo, H., Ha, S., Joseph-McCarthy, D., Kuchnir, L., Kuczera, K., Lau, F. T. K., Mattos, C., Michnick, S., Ngo, T., Nguyen, D. T., Prodhom, B., Reiher, W. E., Roux, B., Schlenkrich, M., Smith, J. C., Stote, R., Straub, J., Watanabe, M., Wiorkiewicz-Kuczera, J., Yin, D., and Karplus, M. (1998) All-atom empirical potential for molecular modeling and dynamics studies of proteins. *J. Phys. Chem. B 102*, 3586−3616.

(41) Ryckaert, J. P., Ciccotti, G., and Berendsen, H. J. C. (1977) Numerical-integration of cartesian equations of motion of a system with constraints: Molecular-dynamics of n-alkanes. *J. Comput. Phys. 23*, 327−341.

(42) Beglov, D., and Roux, B. (1994) Finite representation of an infinite bulk system: Solvent boundary potential for computer-simulations. *J. Chem. Phys. 100*, 9050−9063.

(43) Im, W., Berneche, S., and Roux, B. (2001) Generalized solvent boundary potential for computer simulations. *J. Chem. Phys. 114*, 2924−2937.

(44) Im, W. P., Lee, M. S., and Brooks, C. L. (2003) Generalized Born model with a simple smoothing function. *J. Comput. Chem. 24*, 1691−1702.

(45) Jorgensen, W. L., Chandrasekhar, J., Madura, J. D., Impey, R. W., and Klein, M. L. (1983) Comparison of simple potential functions for simulating liquid water. *J. Chem. Phys. 79*, 926−935.

(46) Nina, M., Beglov, D., and Roux, B. (1997) Atomic radii for continuum electrostatics calculations based on molecular dynamics free energy simulations. *J. Phys. Chem. B 101*, 5239−5248.

(47) Nina, M., Im, W., and Roux, B. (1999) Optimized atomic radii for protein continuum electrostatics solvation forces. *Biophys. Chem. 78*, 89−96.

(48) Hoover, W. G. (1985) Canonical dynamics: Equilibrium phase-space distributions. *Phys. Rev. A 31*, 1695−1697.

(49) Nose, S. (1984) A unified formulation of the constant temperature molecular-dynamics methods. *J. Chem. Phys. 81*, 511−519.

(50) Elstner, M., Porezag, D., Jungnickel, G., Elsner, J., Haugk, M., Frauenheim, T., Suhai, S., and Seifert, G. (1998) Self-consistent-charge

density-functional tight-binding method for simulations of complex materials properties. *Phys. Rev. B 58*, 7260−7268.

(51) Kumar, S., Bouzida, D., Swendsen, R. H., Kollman, P. A., and Rosenberg, J. M. (1992) The weighted histogram analysis method for free-energy calculations on biomolecules. 1. The method. *J. Comput. Chem. 13*, 1011−1021.

(52) Kumar, S., Rosenberg, J. M., Bouzida, D., Swendsen, R. H., and Kollman, P. A. (1995) Multidimensional free-energy calculations using the weighted histogram analysis method. *J. Comput. Chem. 16*, 1339−1350.

(53) Lifson, S., and Jackson, J. L. (1962) On the self-diffusion of ions in a polyelectrolyte solution. *J. Chem. Phys. 36*, 2410−2414.

(54) Zwanzig, R. (1988) Diffusion in a rough potential. *Proc. Natl. Acad. Sci. U.S.A. 85*, 2029−2030.

(55) Roux, B., Allen, T., Berneche, S., and Im, W. (2004) Theoretical and computational models of biological ion channels. *Q. Rev. Biophys. 37*, 15−103.

(56) Menestrina, G. (1986) Ionic channels formed by *Staphylococcus aureus* α-toxin: Voltage-dependent inhibition by divalent and trivalent cations. *J. Membr. Biol. 90*, 177−190.

(57) Harata, N.C., Choi, S., Pyle, J. L., Aravanis, A. M., and Tsien, R. W. (2006) Frequency-dependent kinetics and prevalence of kiss-and-run and reuse at hippocampal synapses studied with novel quenching methods. *Neuron 49*, 243−256.

(58) Weber, T., Zemelman, B. V., McNew, J. A., Westermann, B., Gmachl, M., Parlati, F., Sollner, T. H., and Rothman, J. E. (1998) SNAREpins: Minimal machinery for membrane fusion. *Cell 92*, 759−772.

(59) Sollner, T., Bennett, M. K., Whiteheart, S. W., Scheller, R. H., and Rothman, J. E. (1993) A protein assembly-disassembly pathway in vitro that may correspond to sequential steps of synaptic vesicle docking, activation, and fusion. *Cell 75*, 409−418.

(60) Humphrey, W., Dalke, A., and Schulten, K. (1996) VMD: Visual molecular dynamics. *J. Mol. Graphics 14*, 27−38.